Computational simulation of the PAW-04 nozzle configuration

Juan Hernandez

University of Tennessee at Chattanooga, qmq928@mocs.utc.edu

Recommended Citation

Hernandez, Juan, "Computational simulation of the PAW-04 nozzle configuration" (2019). *Honors Theses.*

Computational Simulation of the PAW-04 Nozzle Configuration

Juan A. Hernandez

Honors College Thesis
The University of Tennessee at Chattanooga

04/05/2019

Dr. Kidambi Sreenivas
Associate Professor
Mechanical Engineering
Thesis Director

Dr. Abdollah (Abi) Arabshahi
Research Professor
Mechanical Engineering
Department Examiner

Abstract

The research was based on the 4th Propulsion Aerodynamics Workshop which was organized by the American Institute of Aeronautics and Astronautics (AIAA) Air Breathing Propulsion System Integration Technical Committee and its objective was to assess the accuracy and numerical prediction capabilities of Computational Fluid Dynamics (CFD). It focused on the work of Behrouzi and McGuirk where they tested two different nozzle configurations under set boundary conditions. The nozzle configurations included a high aspect ratio rectangular nozzle with a clean exit and the same nozzle with an aft-deck attached to the exit. Three different unstructured grids were generated for the clean nozzle using *Pointwise* that varied in refinement and number of points, but only one unstructured grid was generated for the aft-deck. The solver that was used was *Tenasi* and *Fieldview* was used for post-processing.

The first assessment involved testing if the solutions for the clean nozzle were grid independent by comparing Total Pressure values along the axial direction. It was found that the values for the three solutions were between 0.995% and 13.03% from each other. Because of this, the values for the medium definition grid (Grid 2) were compared against the experimental values. This showed that along the centerline, the values for Grid 2 were as accurate as 0.06% from the experimental data up to an x/Dh of 4.5, but beyond that, it went as far as 24.28% from the experimental data. At different cross-sectional planes along the axial direction, the values were between 0.06% and 27%. This meant that the data from the CFD analysis from Grid 2 was good enough to use, especially in the viscous layer at the exit. For the aft-deck configuration, the CFD values matched the experimental data along the centerline up to around x/Dh of 5 but deviates from the experimental data after this point by up to 26.15%. The final test was to compare the static pressure along the surface of the aft-deck. The comparison showed that the surface domain for the aft-deck was viscous enough that the solution converged into the experimental solution.

Acknowledgements

Table of Content

I.   Introduction

The 4th Propulsion Aerodynamics Workshop (PAW04) was organized by the American Institute of Aeronautics and Astronautics (AIAA) Air Breathing Propulsion System Integration Technical Committee and its objective was to assess the accuracy and numerical prediction capabilities of Computational Fluid Dynamics, or CFD, and modeling techniques by simulating the steady-state aerodynamics of nozzle flow. CFD will be used to acquire different values for the flow characteristics of two different nozzle configurations. The values obtained will then be compared to experimental data which was provided by the AIAA Committee [1].

The test conditions and the nozzle geometry provided for this study were based on the experimental work of Behrouzi and McGuirk [2]. They conducted a study to test how the underexpanded supersonic jet plumes of a high-aspect ratio (width divided by length) convergent rectangular nozzle is affected by the presence of an aft-deck, whose purpose is to minimize plume separation from the line of flow. They also tested to find what the optimal length for the aft-deck should be. They tested the same nozzle geometry with and without the aft-deck at nozzle pressure ratios between 1.9 and 4 and used Schlieren visualization, pitot probe, and Laser Doppler Anemometry measurements to capture the behavior of the flow.

II.   Background

A. What is CFD?

Throughout the centuries, there have been two standard approaches for solving complicated fluid dynamics problems. The first and most straightforward approach is experimental. It consists of setting up the desired problem in a controlled environment, then, using what is known about the

problem and changing one of the parameters to see the behavior the variable that is being measured [3]. This method is usually seen as the most accurate model of the behavior of the experiment but can only be trusted if the error is well mitigated and enough tests are performed. The issue with this method is that it usually requires significant resources, such a large budget and a high amount of manpower to mimic the flow behaviors. For instance, to be able to run a wind tunnel experiment on an airplane model, the engineer needs to build a model that has all the detail that will be present in the original design while at the same time, keeping it small enough to allow for the smallest wind tunnel possible that requires a blockage ratio of less than 3%. Also, they must ensure that the flow parameters such as Mach number and Reynold's number match the conditions that the full-scale model will be subjected to so that the data can be useful. This means that they might have to change the working fluid to something that will model the desired conditions [4].

The second approach is theoretical. This usually consists of coming up with models for the behavior of the flow using previous analysis and experimental data. This method will give you a best-case scenario and will be based on certain assumptions and boundary conditions that are hard to find in real-world application; this is useful because they can be used as a rough estimate of the data to get an idea of the behavior of the experiment without having to spend a lot of resources [3]. The third approach used in fluid dynamics is computational, or numerical, also referred to as Computational fluids dynamics (CFD). CFD was developed in the 1960s and 1970s to satisfy the needs of the growing aerospace research community. By using computing power to solve complex algorithms, it enables the researcher to mimic an experimental environment to get the three-dimensional data that is acquired from doing experiments. The advantage of using CFD over the other two research methods is that with the computing power available today the tests can be performed in a fraction of the time compared to going the experimental route, and the use of

resources, such as money and building material, is highly decreased. Also, when it would take a 40 ft wind tunnel to test a 4 ft airplane model, the same values can be obtained using a CFD solver in a mid-size computer tower, which means that it can be run remotely from anywhere compared to having a stationary wind tunnel. However, CFD does not fully replace the need for experimental testing because true data is still required to prove that the model is valid; but it does provide good information for modeling purposes so that instead of physically testing every idea, the researcher can narrow it down to one or two prototypes, using CFD analysis, that can then be tested experimentally [5].

B. How does CFD work?

CFD analysis is essentially a computer program that solves the Navier-Stokes equations and fluid dynamic principles to calculate different fluid characteristics at specified boundary conditions and inlet conditions using finite difference, volume, and element techniques [3]. There are three stages to solving a fluid problem using CFD. The first step is pre-processing, which consist of defining the geometry and building the domain. Second is solving the problem using the generated domain, and third is post-processing, where the results can be visualized, and numerical data can be obtained [5].

In the pre-processing stage, the first step consists of defining the geometry, or model. This means that a well-defined shell model needs to be made water-tight, i.e., the connections are sealed with tolerances on up to 10^{-3} to prevent 'leaks' during the solving process. The solution to the flow problem is defined at nodes that make up the cell that cover the domain. The more cells generated, the better the solution will be. Because of the importance of the quality of the mesh, over half of the time doing CFD analysis is dedicated to grid generation [5]. There are two common types of

grids, which are structured and unstructured. A structured grid is one where the cells, which are quadrilateral (2D) or hexahedra (3D), are arranged so that the neighboring cells are known implicitly. In other words, they have a set structure that is carried out from the body to the farfield of the domain providing coordinate surfaces. The grid points are identified as the points of intersection of curvilinear lines that form the surfaces. [6]
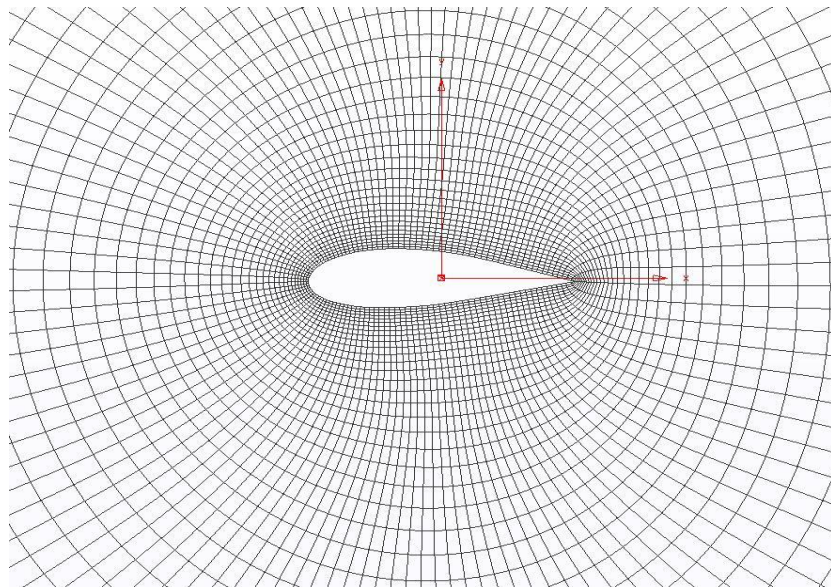
Figure 1 – Sample Structured 2-D Grid on an Airfoil

Figure 1 shows the basic surface of a structured grid. It has a small spacing and high definition close to the boundary of the airfoil and the leading edge, but the areas of the quadrilaterals increase as it grows away from the surface. Some of the mathematical methods used to generate structured grids include transfinite interpolation, which uses a set of algebraic equations to compute the location of each interior point based on the location of the boundary grid point for that line. Structured grids can also be generated using elliptic partial differential equations and interior control functions. Some of the advantages of using structured grids are that they provide high-quality cells that can help with getting a much better solution in the viscous layer, they converge

better than unstructured which means that they can produce more accurate results, and their well-defined computational direction normal allow for the boundary conditions and turbulence models to work well [7].

On the other hand, unstructured grids are generated in a more adaptive manner, where the pattern in which the points are connected differs from point to point. Instead of using quadrilateral or hexahedron, unstructured grids use triangles and tetrahedron to fill up the domain rapidly. [6]
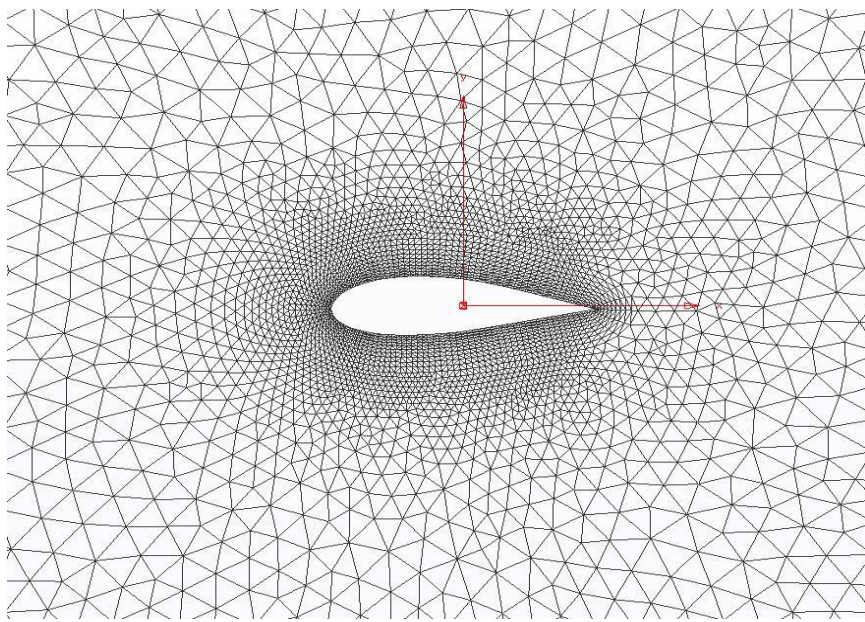
Figure 2 – Unstructured grid on Airfoil

Unstructured grids are generated using two different methods: Delaunay triangulation, shown in figure 2, and the Advancing Front method. To be able to get a good definition in the boundary layer, however, unstructured grid generation uses anisotropic tetrahedral extrusion (T-Rex). T-Rex works by distributing points around the specified parameter, and then extruding (or advancing) the boundary points one at a time towards the farfield. The layers advance until specified with a set growth rate or until they start to collide, and then the rest of the domain is filled with Delaunay or

Advancing front isentropic layers. Some of the advantages in using unstructured techniques is that the grids are generated at a much faster rate than structured because once the boundary layer is specified, the software will fill up the extra space with arbitrary tetrahedron and prisms, as well as taking less computational resources to solve. They are also easier to use when generating grids for complex geometries [7].

The second step to CFD is solving the problem. There are three techniques used for the discretization of numerical solutions. The first is the finite difference method which uses the Taylor series and replaces the partial derivatives at each point in the domain with approximate algebraic difference equations, which are solved either iteratively or simultaneously. One advantage of using this method is that it is easy to implement, but it is restricted to structured grids and does not conserve momentum, energy, and mass. In finite element solutions for a viscous flow problem, the flow-field parameters of velocity and temperature are calculated at all the grid points [3]. The finite element method is a numerical technique that uses simple piecewise functions to describe the local change in flow variables at each node. From this, a set of algebraic equations are obtained for unknown coefficients of the approximating functions. This method is mostly used for structural analysis. The final method is the finite volume method. The numerical algorithm consists of integrating the governing fluid flow equations over all the control volumes that make up the solution domain. Its discretization involves using finite difference type approximations to use in the integrated equations which convert the integral into a system of algebraic equations. Then, the solution for each control volume is solved using iteration [4].

After solving the flow problem, the final step is the post-processing stage. This step is used to visualize the problem. It includes creating 2D and 3D surface plots, particle tracking, line and

shaded contour plots, and fluid behaviors. Also, data can be tabulated into tables and graphs at different locations throughout the control volume can be created [4].

C. Governing Fluid Equations

Fluid flow is governed by three coupled partial differential equations: the continuity, momentum, and energy equations. Continuity is based on the conservation of mass principle, momentum is based on Newton's second law that states that force equals mass multiplied by acceleration and the conservation of energy.

The fundamental principle of mass conservation in a finite control volume is that the net flow out of the control volume through a surface equals to the time rate of decrease of mass inside the control volume. To break this into components, the mass flow of a fluid across the surface is

$$\dot{m} = \rho V * dS \tag{1}$$

where $\dot{m}$ is equal to the mass flow rate, ρ is the density of the fluid, **V** is the velocity normal to the surface, and **dS** is the elemental surface area. Note that **dS** and **V** always point out of the control volume, making the mass flow rate positive when it is an outflow. In the limit where the net mass flow out is the summation over S of the elemental mass flow, equation 1 becomes a surface integral, where

$$B = \oiint_S \rho \vec{V} * d\vec{S} \tag{2}$$

Equation 2 equals the net flow out of the control volume (C.V.) through surface S. Now considering the right side of the conservation of mass principle, the mass contained within the elemental volume d∀ is ρd∀. This means that the total mass inside the control volume is

10

$$\oiiint_V \rho * d\Psi \tag{3}$$

From this, the time rate change of mass inside the control volume is

$$C = \frac{-\partial}{\partial t} \oiiint_V \rho * d\Psi \tag{4}$$

Combining equations 2 and 3, the conservation form of the continuity equation can be written as

$$\frac{\partial}{\partial t} \oiiint_V \rho * d\Psi + \oiint_S \rho V * dS = 0 \tag{5}$$

Using Gauss divergence theorem, this can be written as

$$\frac{\partial \rho}{\partial t} + \rho \vec{V} \bullet \vec{V} = 0 \tag{6}$$

where equation 5 is the continuity equation in partial differential form. Also, the product of $\nabla \bullet V$ is a physical representation of the time rate of change of the volume of a moving fluid element, per unit volume.

Newton's second law states that the rate of change of momentum of fluid equals the sum of the forces on the particle. Looking at the x-axis only, this can be written as

$$\sum \vec{F} = m\vec{a} \tag{7}$$

$\vec{F}$ is the force exerted on the particle, m is the mass of the particle, and $\vec{a}$ is the acceleration. Equation 6 is the momentum equation, which can be written in the more general form

$$\vec{F} = \frac{d}{dt}(m\vec{V}) \tag{8}$$

11

The product $m\vec{V}$ is the momentum of a body with constant mass. The forces exerted on the fluid as it flows through the control volume come from two different sources. The first are body forces, which include gravity, electromagnetic forces, or any other forces which "act at a distance" inside the control volume. The second source is from surface forces like pressure and shear stress acting on the control surface, **S**. The body and surface forces can be modeled by the following, looking at the x-direction only:
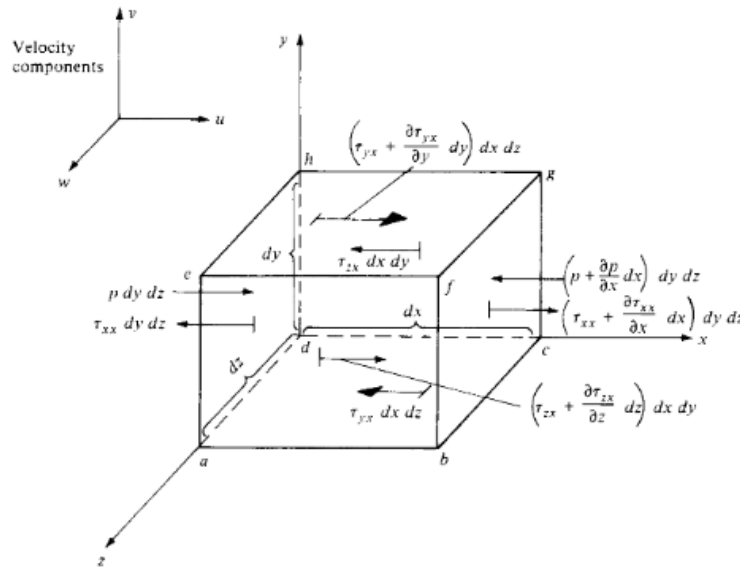
Figure 3-Infinitesimally small, moving fluid element [3]

The net force on the fluid element in the x-direction can be written as,

$$F_x = \left[p - \left(p + \frac{\partial p}{\partial x} dx\right)\right] dydz + \left[\left(\tau_{xx} + \frac{\partial \tau_{xx}}{\partial x}\right) - \tau_{xx}\right] dydz$$
$$+ \left[\left(\tau_{yx} + \frac{\partial \tau_{yx}}{\partial y}\right) - \tau_{yx}\right] dxdz + \left[\left(\tau_{zx} + \frac{\partial \tau_{zx}}{\partial z}\right) - \tau_{zx}\right] dxdy$$

(9)

which is further simplified to be

$$F_x = \left(\frac{-\partial p}{\partial x} + \frac{\partial \tau_{xx}}{\partial x} + \frac{\partial \tau_{yx}}{\partial y} + \frac{\partial \tau_{zx}}{\partial z} \right) dx\,dy\,dz \tag{10}$$

Equation 9 represents the left-hand side of the momentum equation, Equation 6. From shear and normal stress principles, $\tau_{xx}, \tau_{yx}, \tau_{zx}$ are said to be,

$$\tau_{xx} = \frac{-2}{3} \mu (\nabla \cdot V) + 2\mu \frac{\partial u}{\partial x} \tag{11}$$

$$\tau_{yx} = \mu \left(\frac{\partial v}{\partial x} + \frac{\partial u}{\partial y} \right) \tag{12}$$

$$\tau_{zx} = \mu \left(\frac{\partial u}{\partial z} + \frac{\partial w}{\partial x} \right) \tag{13}$$

In equations 10 to 12, μ is the dynamic viscosity of the fluid, and u, v, and w are the velocities in the x, y, and z-directions, respectively. Also, the mass of the fluid element is equal to

$$m = \rho\,dx\,dy\,dz \tag{14}$$

And the acceleration in the x-direction is simply the rate of change of u with respect to time, which means that

$$a_x = \frac{du}{dt} \tag{15}$$

since u is a function of x, y, z, and t the chain rule must be applied, i.e.,

$$\frac{du}{dt} = \frac{\partial u}{\partial t} + u\frac{\partial u}{\partial x} + v\frac{\partial u}{\partial y} + w\frac{\partial u}{\partial z} \tag{16}$$

Combining equations 9 to 16 into Equation 17, the Navier-Stokes equation in the x-direction is written as

$$\rho\left(\frac{\partial u}{\partial t} + u\frac{\partial u}{\partial x} + v\frac{\partial u}{\partial y} + w\frac{\partial u}{\partial z}\right) = \frac{-\partial p}{\partial x} + \frac{\partial}{\partial x}\left(\frac{-2}{3}\mu(\nabla \cdot V) + 2\mu\frac{\partial u}{\partial x}\right) +$$

$$\frac{\partial}{\partial y}\left[\mu\left(\frac{\partial v}{\partial x} + \frac{\partial u}{\partial y}\right)\right] + \frac{\partial}{\partial z}\left[\mu\left(\frac{\partial u}{\partial z} + \frac{\partial w}{\partial x}\right)\right] \tag{17}$$

The same approach applies to the y and z-directions, thus

$$\rho\left(\frac{\partial v}{\partial t} + u\frac{\partial v}{\partial x} + v\frac{\partial v}{\partial y} + w\frac{\partial v}{\partial z}\right) = \frac{-\partial p}{\partial y} + \frac{\partial}{\partial y}\left(\frac{-2}{3}\mu(\nabla \cdot V) + 2\mu\frac{\partial v}{\partial y}\right) +$$

$$\frac{\partial}{\partial x}\left[\mu\left(\frac{\partial v}{\partial x} + \frac{\partial u}{\partial y}\right)\right] + \frac{\partial}{\partial z}\left[\mu\left(\frac{\partial v}{\partial z} + \frac{\partial w}{\partial y}\right)\right] \tag{18}$$

$$\rho\left(\frac{\partial w}{\partial t} + u\frac{\partial w}{\partial x} + v\frac{\partial w}{\partial y} + w\frac{\partial w}{\partial z}\right) = \frac{-\partial p}{\partial w} + \frac{\partial}{\partial w}\left(\frac{-2}{3}\mu(\nabla \cdot V) + 2\mu\frac{\partial w}{\partial z}\right) +$$

$$\frac{\partial}{\partial y}\left[\mu\left(\frac{\partial v}{\partial z} + \frac{\partial w}{\partial y}\right)\right] + \frac{\partial}{\partial x}\left[\mu\left(\frac{\partial u}{\partial z} + \frac{\partial w}{\partial x}\right)\right] \tag{19}$$

Equations 16 to 18 represent the complete Navier-Stokes equations in the conservation form for an unsteady, compressible, three-dimensional viscous flow.

Looking at conservation of energy ideas, the first law of thermodynamics states that the rate of change of energy inside the fluid element equals the net flux of heat into element plus the rate of work done on the element due to body and surface forces. Using the same shear stress models as in Figure 3, the rate of work done on the element due to body and surface forces is given by

$$\delta W = -\left[\left(\frac{\partial(up)}{\partial x} + \frac{\partial(vp)}{\partial y} + \frac{\partial(wp)}{\partial z}\right) + \frac{\partial(u\tau_{xx})}{\partial x} + \frac{\partial(u\tau_{yx})}{\partial y} + \frac{\partial(uz)}{\partial z} + \frac{\partial(v\tau_{yy})}{\partial y}\right.$$
$$\left. + \frac{\partial(v\tau_{xy})}{\partial x} + \frac{\partial(v\tau_{zy})}{\partial z} + \frac{\partial(w\tau_{zz})}{\partial z} + \frac{\partial(w\tau_{xz})}{\partial x} + \frac{\partial(w\tau_{yz})}{\partial y}\right] dxdydz$$
$$+ \rho f \cdot V dxdydz \tag{20}$$

Furthermore, using Fourier's law of heat conduction, the net flux of heat into the element is equal to

$$\delta q = \left[\rho\dot{q} + \frac{\partial}{\partial x}\left(k\frac{\partial T}{\partial x}\right) + \frac{\partial}{\partial y}\left(k\frac{\partial T}{\partial y}\right) + \frac{\partial}{\partial z}\left(k\frac{\partial T}{\partial z}\right)\right]dxdydz \qquad (21)$$

where k is the thermal conductivity, and $\dot{q}$ is the heat flux. Combining equations 19 and 20, and doing some manipulation using the momentum and continuity equations, the rate of change of energy inside the fluid element is represented by

$$\begin{aligned}\frac{\partial(pe)}{\partial t} + \nabla\cdot(\rho eV) = {}& \rho\dot{q} + \frac{\partial}{\partial x}\left(k\frac{\partial T}{\partial x}\right) + \frac{\partial}{\partial y}\left(k\frac{\partial T}{\partial y}\right) + \frac{\partial}{\partial z}\left(k\frac{\partial T}{\partial z}\right) - p\left(\frac{\partial u}{\partial x}+\frac{\partial v}{\partial y}+\frac{\partial w}{\partial z}\right) - \frac{2}{3}\mu\left(\frac{\partial u}{\partial x}+\frac{\partial v}{\partial y}+\frac{\partial w}{\partial z}\right)^2 \\ & + \mu\left[2\left(\frac{\partial u}{\partial x}\right)^2 + 2\left(\frac{\partial v}{\partial y}\right)^2 + 2\left(\frac{\partial w}{\partial z}\right)^2 + \left(\frac{\partial u}{\partial y}+\frac{\partial v}{\partial x}\right)^2 + \left(\frac{\partial u}{\partial z}+\frac{\partial w}{\partial x}\right)^2 + \left(\frac{\partial w}{\partial y}+\frac{\partial v}{\partial z}\right)^2\right]\end{aligned} \qquad (22)$$

Equation 21 is the energy equation in conservative form, where e is the internal energy [3].

III. Numerical Simulation

A. Geometry and Mesh

The nozzle provided for the experiment was a high aspect ratio (7.35) rectangular nozzle with a round inlet. The first configuration, which is referred to as the Baseline Nozzle, has an inlet diameter of 54 mm and an 81mm long round to rectangular transition to the rectangular exit of 93.8mm by 12.76mm with the trailing edge lip thickness is 0.5mm. for this nozzle, the hydraulic diameter, D_h is 22.46mm, which is obtained from the height and width of the outlet and is used as a way to analyze a rectangular cross section as if it was round.
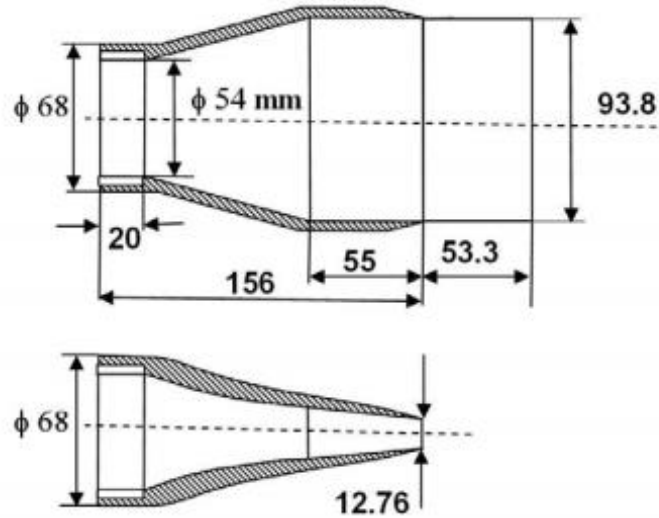
Figure 4 – Nozzle configuration and dimensions

The second configuration has the same inlet and outlet characteristics as the Baseline nozzle but includes a 53.3 mm long aft-deck downstream of the nozzle secured by a collar around the nozzle exit. [1]

There were four unstructured grids created for the experiment using a grid generation software called *Pointwise*. It is a meshing software that is known for giving the user full control of the grid using their T-Rex technique to create unstructured grids with a resolved boundary layer. The first grid is using the baseline nozzle geometry. It has a total of 4,042,265 points and a spacing of 0.2 at the nozzle exit which grows as it gets further. There was a separate block created at the front of the exit to create a viscous region so that the behavior of the flow could be better predicted in this area. The viscous block for grid 1 consists of 2,052,151 points of the total number of points.
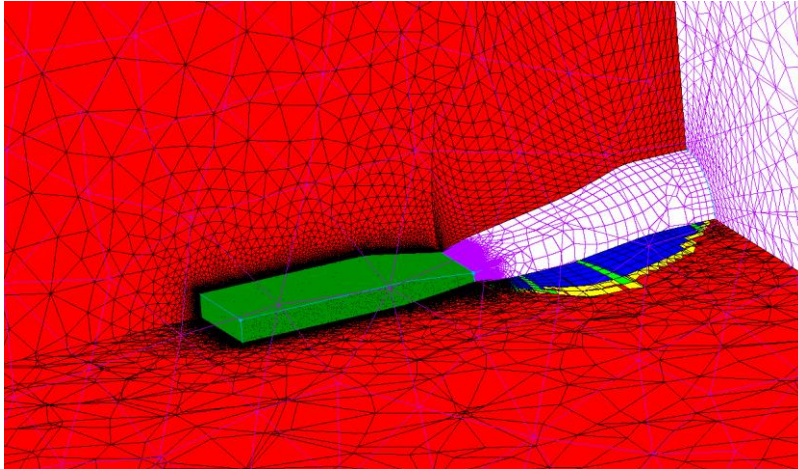
Figure 5- Grid 1 for the Baseline Nozzle Configuration

Grid 2 and Grid 3 were created using a glyph script in *Pointwise* that allowed the refinement of Grid 1 by 1.5 and 1.75. This minimized the time it took to create an entirely new grid by letting the script do the work using similar parameters. From this, Grid 2 came out with a total of 11,092,357 points, a spacing of 0.133 at the nozzle exit, and 5,849,198 points in the viscous block. Grid 3 was solved to have 20,104,791 total points, a spacing of 0.107 at the nozzle exit, and 8,836,933 points in the viscous block. Looking at figure 6, it can be seen how concentrated the points are at the front of the nozzle exit on Grid 3 because that is the area of interest for the data that needs to be collected.
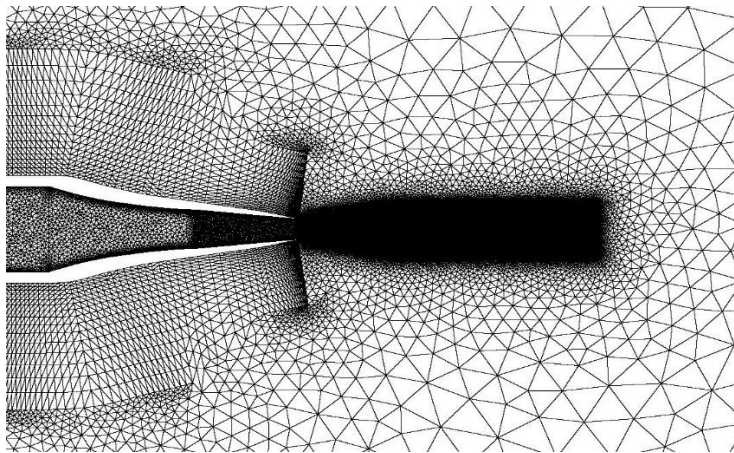
Figure 6 – Y-plane cell profile for Grid 3

For the aft-deck geometry configuration, only one unstructured grid was generated. This was a very fine mesh with a nozzle exit spacing of 0.02 and a total of 11,621,968 points. The deck was defined by using a viscous block with 918,761 points. To refine the region after the aft-deck, a technique for meshing wings was used that incorporates a two-dimensional wake domain that is attached to the trailing edge of the wing, or in this case the edge of the deck. T-Rex uses this domain to grow from it at a specified rate. This can be seen in figure 7 by how concentrated the cells are at the deck and the wake domain.
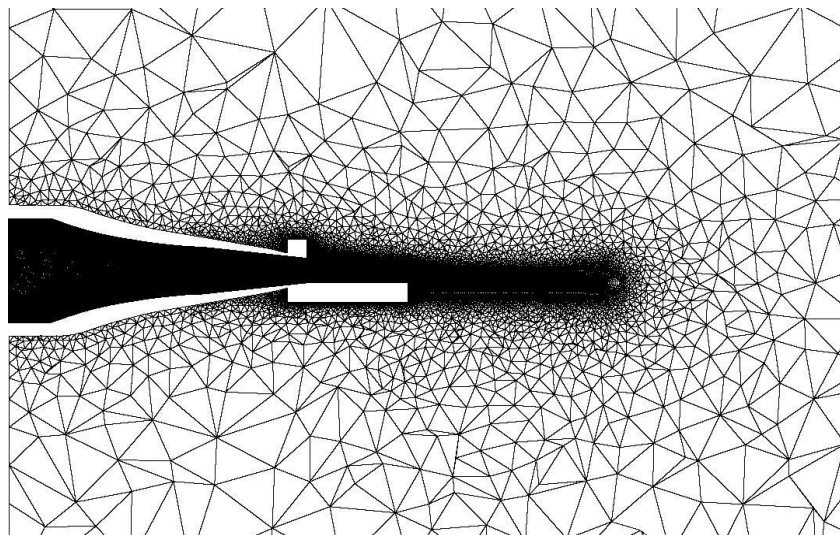
Figure 7 – Unstructured Grid for Aft-Deck Geometry Configuration

B. Boundary Conditions

The boundary conditions that were used consist of a static freestream with ambient pressure and temperatures 14.46 psi and 504 R. The solver used ideal gas equations and properties of air that include γ of 1.4, a universal gas constant of 53.35 ft•lbf/lbm•R, and an acceleration due to gravity of 32.174 ft/sec^2. Also, the nozzle inflow temperature was set to ambient temperature, and

adiabatic, no-slip wall conditions for all nozzle walls. The tests were done at a constant NPR of 3.5 because this seemed to be where the nozzle best performed.

The results that the committee expected include total pressure along the nozzle exit geometry centerline, major and minor axes for both the baseline configuration and the aft-deck. Also, static pressure along the surface of the deck for the aft-deck configuration only [1].

C. Flow Solver

The solver that was used is called *Tenasi*. It is a node-centered, finite volume, implicit scheme applied to general unstructured grids with nonsimplical elements. The flow variables are stored at the vertices and surface integrals are evaluated on the median dual surrounding each of these vertices. An important distinguishing feature of *Tenasi* is that the same executable can be used solve different sets of governing equations, i.e., incompressible, compressible, preconditioned, surface capturing, etc. by choosing a flow regime at runtime. The inviscid fluxes are evaluated using either a Roe-averaged, flux-difference split approach or an HLLC approach, while the viscous fluxes are evaluated using a directional derivative approach. Higher order accuracy is achieved through the use of variable extrapolation with the gradients appearing in the reconstruction being evaluated using an unweighted least squares approach. The gradients appearing in the viscous fluxes are evaluated using a weighted least squares approach. The turbulence models available in the flow solver include the one equation Spalart-Allmaras model, the one equation Menter SAS model, the two equation k-ε model and the two equation k-ω/k-ε hybrid model (baseline and SST variants) and an assortment of Reynolds-stress and LES models. These models are loosely coupled with the mean flow. The parallel solution procedure consists of a scalable solution algorithm implemented to run efficiently on grid subdomains distributed across

multiple processes and communicating through MPI. The algorithm has multiple nested kernels viz. time step, Newton iteration, LU/SGS iteration etc., and the subdomain coupling is at the innermost level, i.e., in the solution of the linear system. A block-Jacobi type updating of the subdomain boundaries ensures efficient parallelization with a small incremental cost incurred in terms of sub-iterations required to recover the convergence rate of the sequential algorithm [8]. For post-processing, the program that was used is called *Fieldview.* It is a software owned by Intelligent Light that allows for data analysis through visualization and tabulated data.

IV. Results

The first analysis of the results was done by comparing the solutions for grids 1, 2, and 3 to see if the refinement of the grids reached convergence. Figure 8 shows the Total Pressure for the grids across the center line in the x-direction at different points compared to the hydraulic diameter.
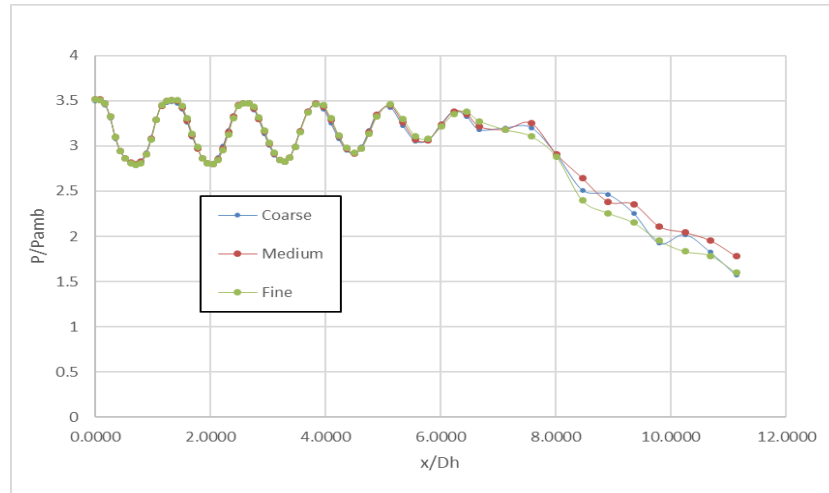
Figure 8 – Pt/Pamb versus x/Dh

Figure 8 shows that across the centerline, the values that were obtained for Grids 1, 2, and 3 match each other until x/Dh of about 6.5 because the largest margin between each grid before this point is 0.955%. after x/Dh of 6.5, the largest error is 11.67%, which occurs at x/Dh of 11.13 because the definition of the grid at this point is not optimal.

Figures 9 and 10 show the comparison of the total pressures for Grids 1, 2, and 3 across vertical and horizontal profiles, respectively, at axial locations of 0.5, 1, 3.5, 5, and 10, where the axial location is recorded in distance from the nozzle exit over hydraulic diameter.
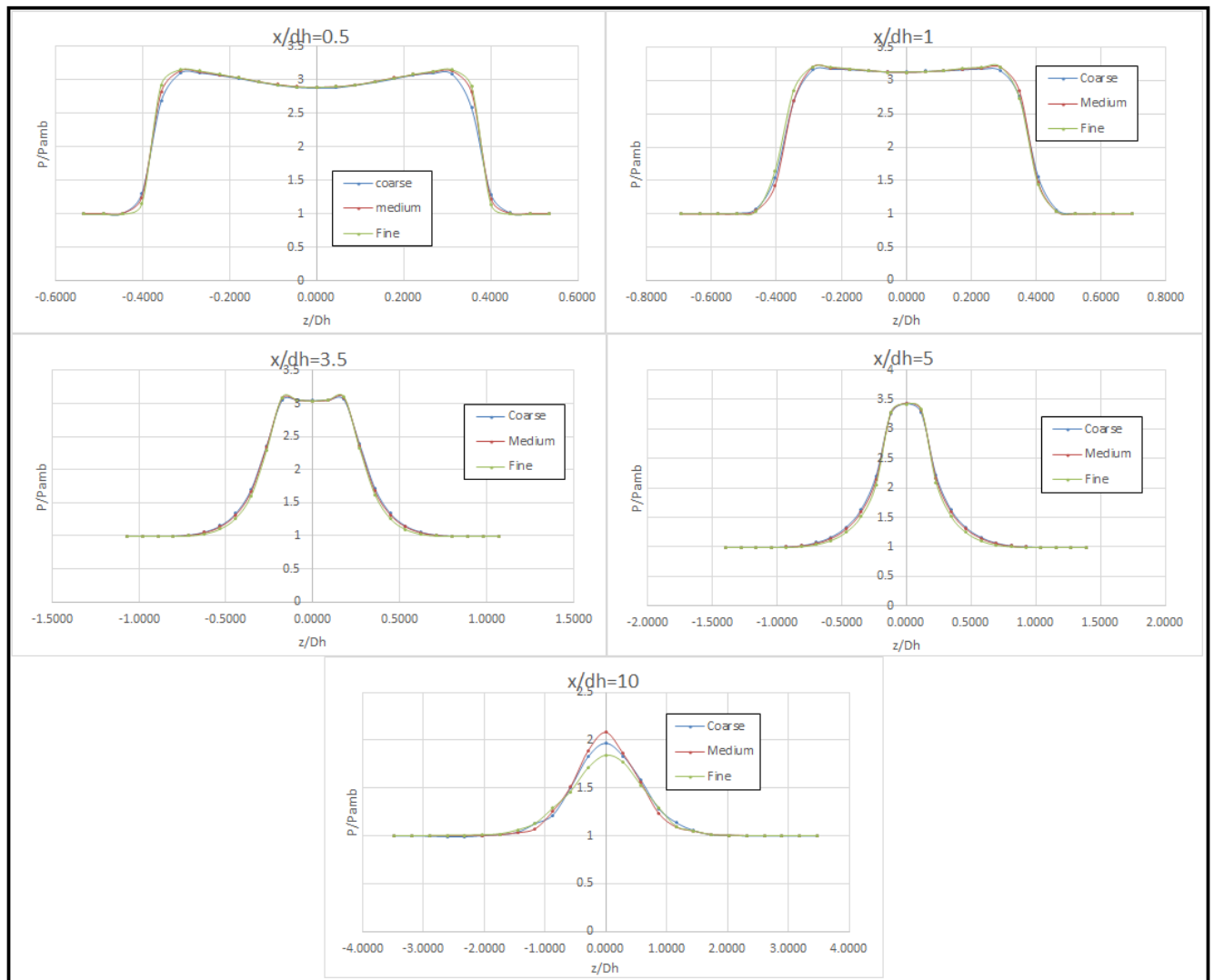
Figure 9 – Pt/Pamb versus z/Dh at different axial locations
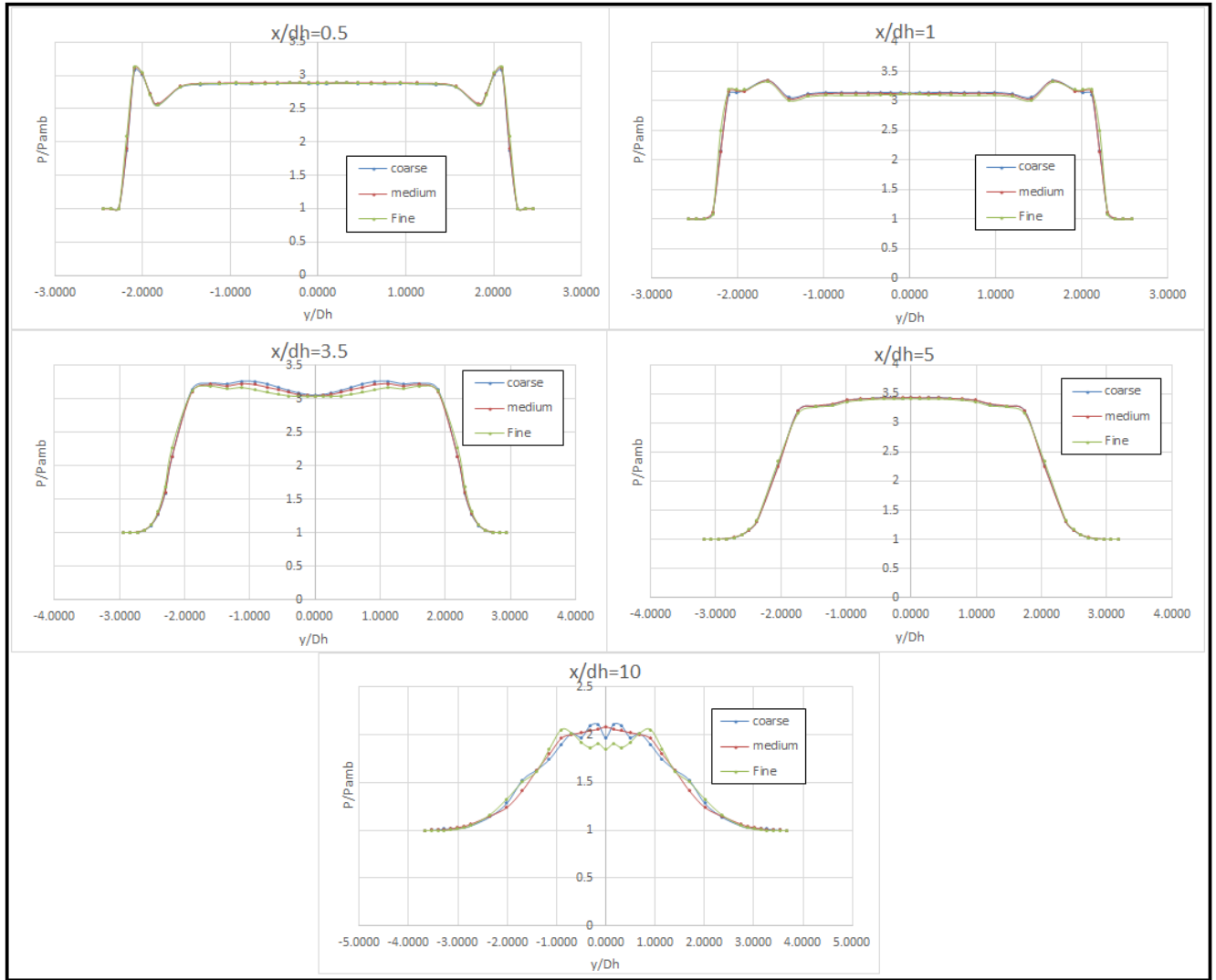
Figure 10 - Pt/Pamb versus y/Dh at different axial locations

Looking at figures 9 and 10, the data collected from grids 1, 2 and 3 does not change very much as the refinement of the mesh increases. The only place where there is a big change in the data collected is at x/Dh of 10 where the deviation between grids 1 and 2 in the horizontal span is as high as 7.54%, and 13.03% between grids 2 and 3 which occurs where y/Dh equals 0. In the vertical span, the biggest change also occurs where y/Dh is 0. These results show that the refinement of the viscous block in the coarse grid is sufficient to attain useful data. However, past that concentrated area, where x/Dh is above 8, more refinement was necessary for grids 1 and 2 to be

able to converge into the best result. Because of this, only grid 2 will be evaluated with the experimental data since it lies in the middle and is very close in values grid 3.

Figure 11 shows the side-by-side comparison of the pressure across the center line for the baseline geometry, while Figures 12 and 13 show the comparison of the total pressures across vertical and horizontal profiles.
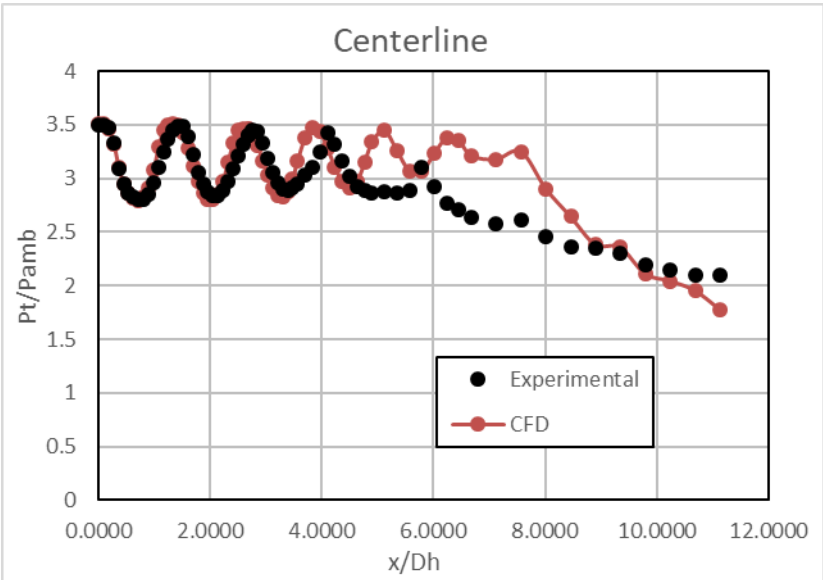
Figure 11 – Pt/Pamb versus x/Dh for Experimental and CFD Data

Between x/Dh of zero and 4.5, both the CFD and experimental Data follow the same path, with the largest error of 11.60% and as accurate as 0.06%. After this point, the CFD values lose the path deviations from the experimental data of up to 24.28%.
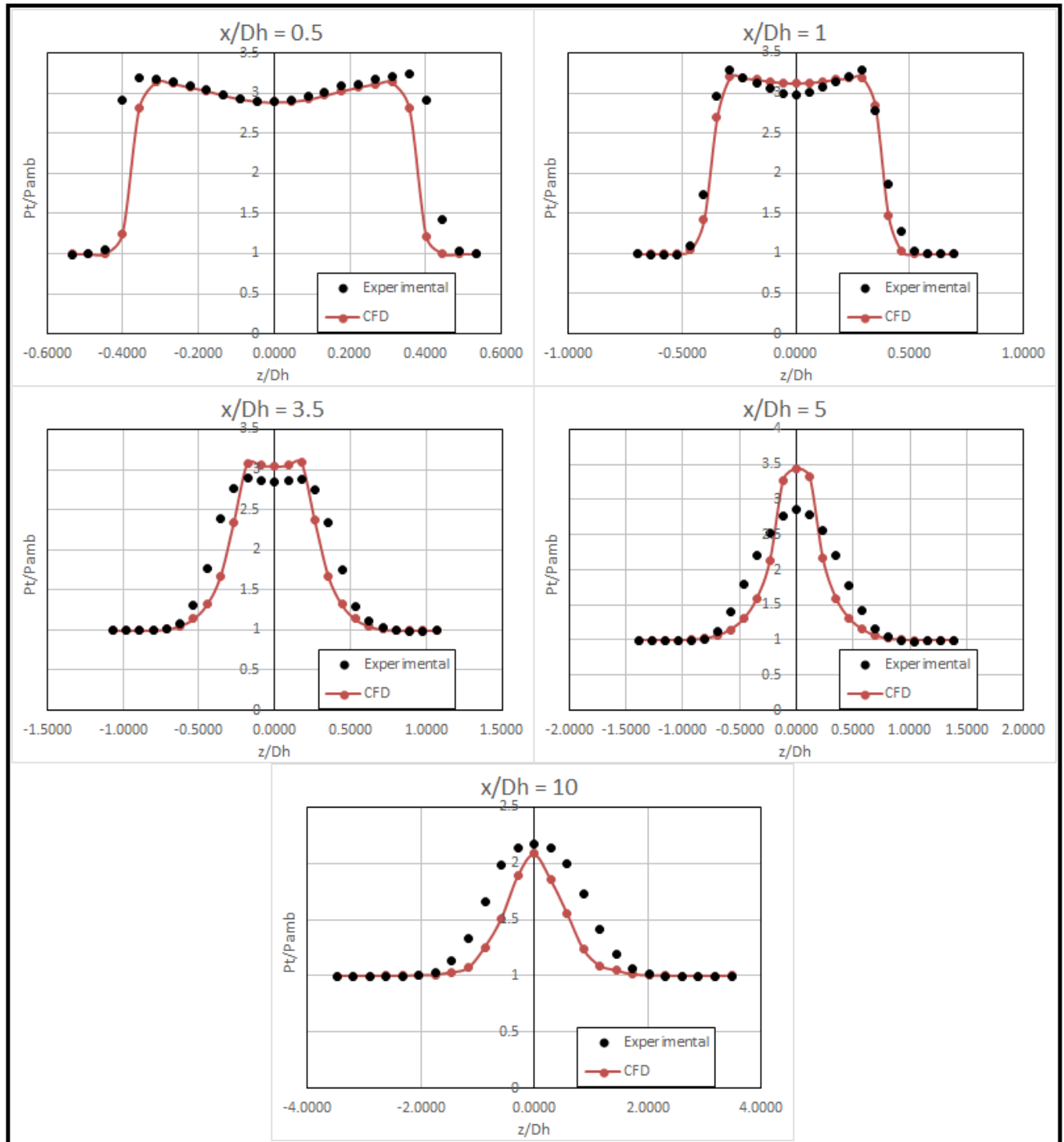
Figure 12 – Pt/Pamb versus z/Dh comparison for Experimental and CFD data
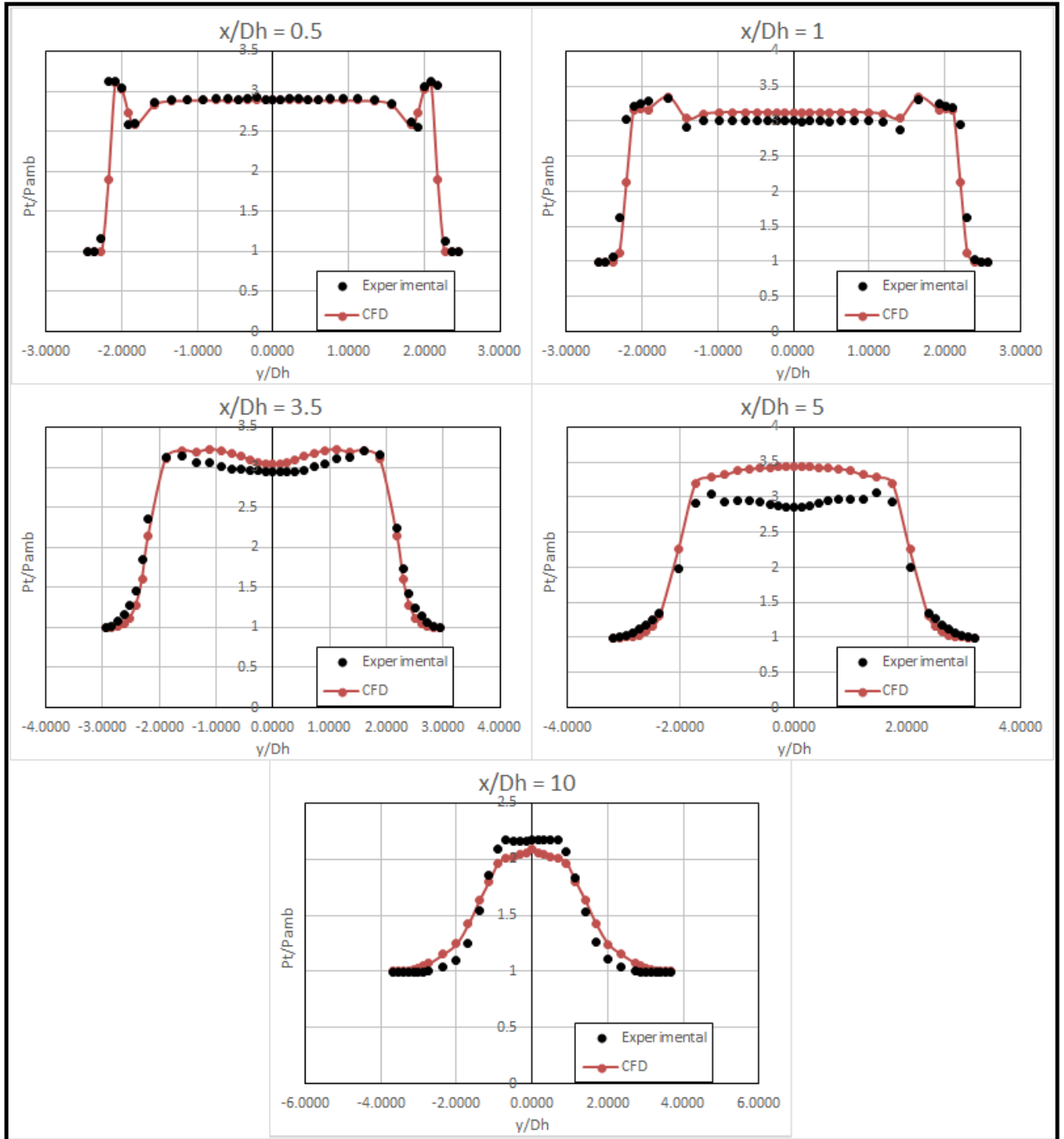
Figure 13 - Pt/Pamb versus y/Dh comparison for Experimental and CFD data

Looking at the horizontal and vertical pressure profiles in figures 12 and 13, the CFD data is more

accurate as the points get closer to the nozzle exit in the axial direction. In figure 12, the values

between z/Dh of -0.2 and 0.2 at x/Dh of 0.5 are a perfect fit to the experimental data with an accuracy of as close as 0.06%. The only location where the data deviates from the experimental values is at x/Dh of 5, where the deviation is between 15% and 27% closer to the centerline. Also, although the data where x/Dh is 5 seem to follow the same path, at some discrete points the CFD data is marginally smaller which could be due to lack of local point at this exact location and the solver was forced to interpolate using the values around it.

Figures 11 through 13 show that the definition of the grid was good to use, especially closer to the nozzle exit. However, when the points were analyzed passed the viscous block, the definition was lost as the points diverged into the farfield and the solver could not converge into the correct value. Furthermore, since only one grid was solved for the aft-deck nozzle geometry, the CFD data from that grid will be compared directly to the experimental data. Figure 14 shows the comparison between the experimental data and the CFD data across the center line.
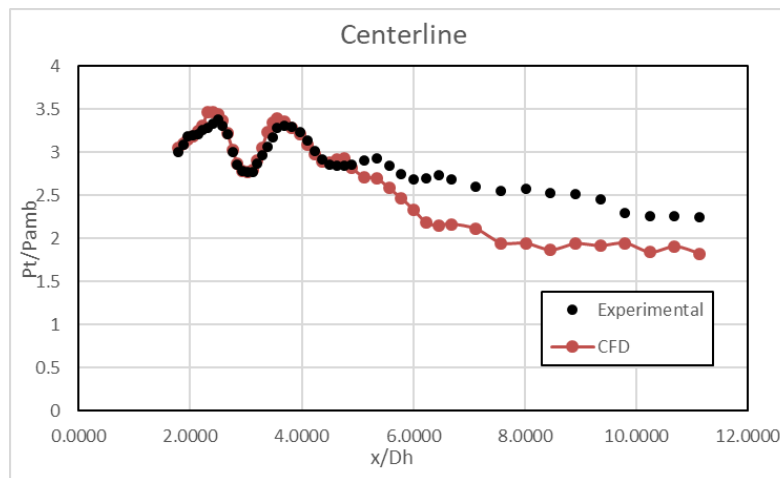
Figure 14 – Pt/Pamb versus x/Dh comparison for Aft-Deck Configuration

The CFD data matches the experimental data across the centerline, although it separates at around x/Dh of 5 but still follows the same behavior. The largest percent error is 26.15% and occurs at x/Dh of 8.46.
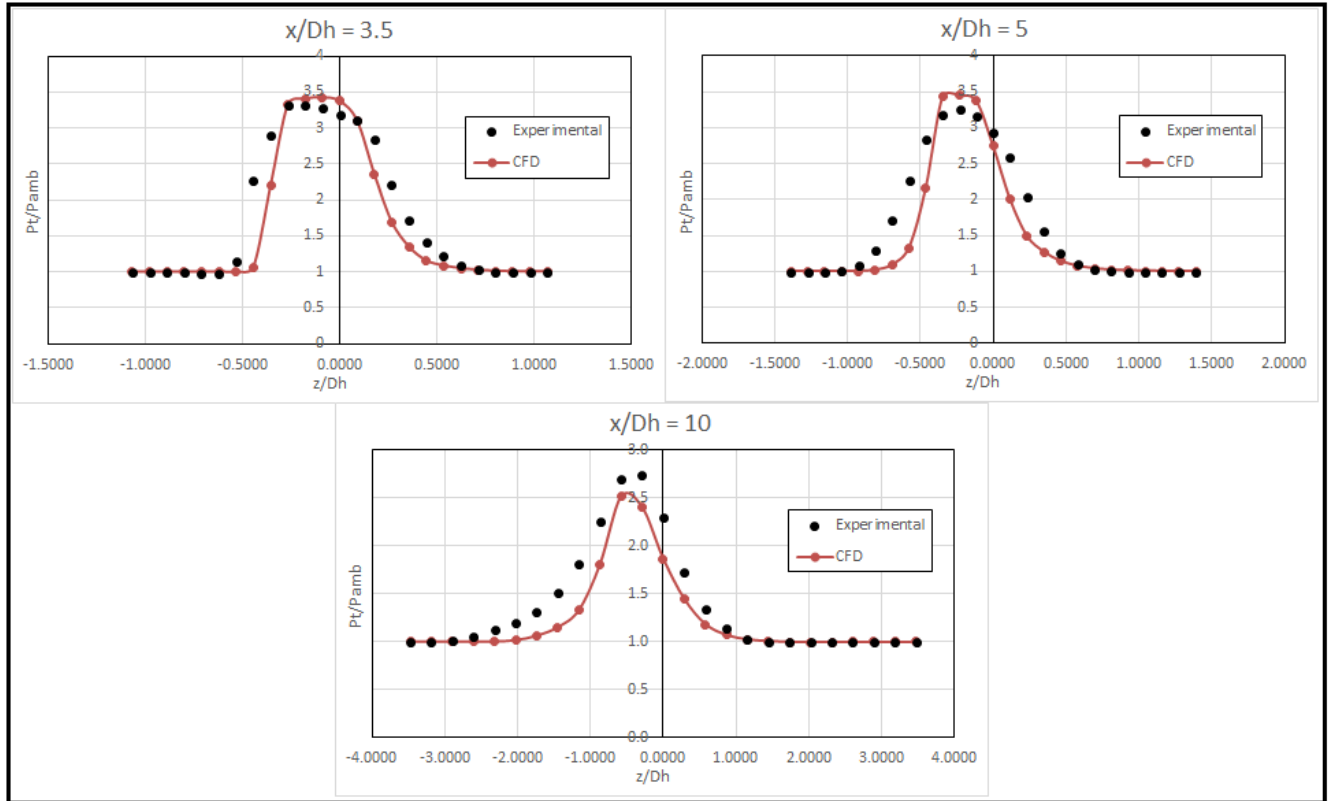
Figure 15 – Pt/Pamb versus z/Dh for Aft-Deck Configuration

From Figure 15, the CFD data is slightly off the experimental data. At x/Dh of 5 the Pressure distribution from the CFD data has a larger peak, but fat x/Dh of 10 it has a lower peak. The largest error recorded in the vertical span for all three locations was 53.36%, which occurs when z/Dh equals -0.4452 at x/Dh of 3.5. This occurred because there were some issues with T-Rex as it built the viscous block in the area closer to the surface of the deck.
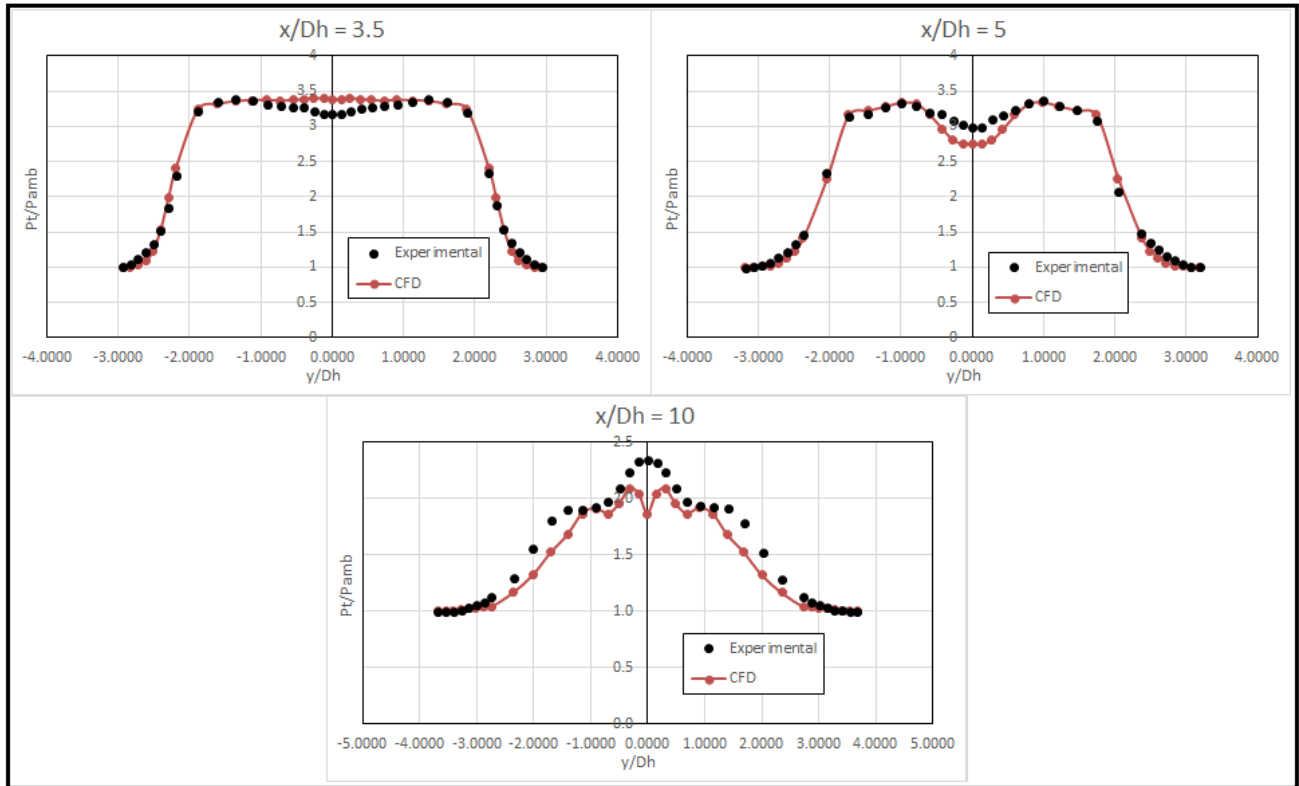
Figure 16 – Pt/Pamb versus y/Dh for Aft-Deck Configuration

From Figure 16, the CFD data is off as it approaches the center line but fits the experimental data throughout, especially at x/Dh of 3.5 and 5. At x/Dh of 10, however, the CFD values are offset from the experimental values with errors of up to 20.56%, while the largest error at 3.5 and 5 is only about 10%.

The final validation test that was asked for by the committee was to compare the static pressure at 11 different points on the surface of the deck, which is shown in figure 17 below.
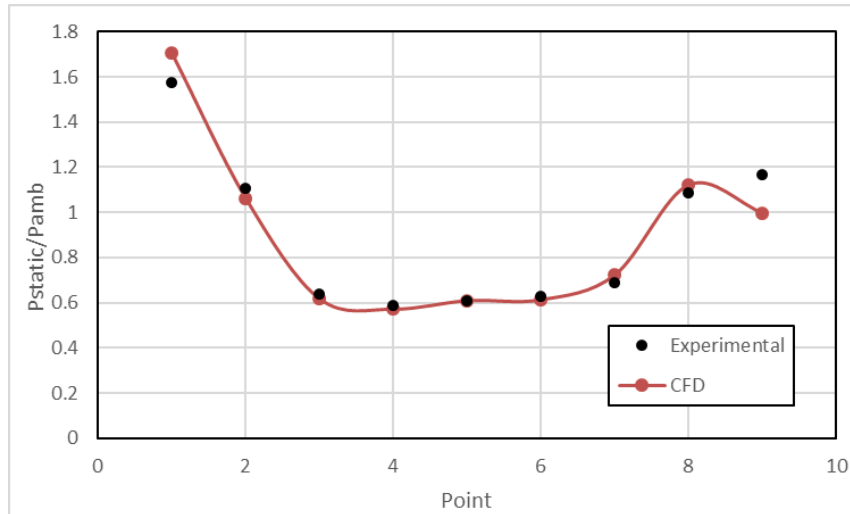
Figure 17 – Static Pressure distribution across Aft-Deck

The static pressure distribution throughout the aft-deck shown in figure 17 shows that the refinement of the surface domain on the deck was enough to get accurate values, with the largest deviation of 14% occurring close to the corner of the deck.

V.   Conclusion

The research involved comparing CFD data for two different configurations to the data acquired by the studies done by Behrouzi and McGuirk. Their work included two different nozzle configurations; one with a clean exit, and one with an aft-deck attached to the exit. The parameters that they evaluated included Total Pressure along the axial direction of the nozzle exit for both configurations and static pressure along the surface of the aft-deck. The CFD analysis included three different unstructured grids for the baseline nozzle, which varied in refinement from coarse to fine, and one unstructured grid for the aft-deck. The solver used, called *Tenasi*, is a node-centered, finite volume, implicit scheme applied to general unstructured grids with nonsimplical elements that allows the same executable to be used to solve different sets of governing equations,

i.e., incompressible, compressible, preconditioned, surface capturing, etc. by choosing a flow regime at runtime. The data extraction and post-processing was done by using *Fieldview* and scripts that were provided.

The first analysis involved comparing the data from Grids 1, 2, and 3 for the baseline configuration to test if the solutions were grid independent. It was determined that although each grid had a significantly higher number of points than the other, the data was close between them with deviations between each grid of as low as 0.02% between Grids 2 and 3 but as high as 13.03% between Grids 1 and 2. This means that at the definition of Grid 1, the mesh was reaching convergence, especially in the viscous region at the front of the nozzle exit. However, since the gap was smaller between Grids 2 and 3, Grid 2 was chosen to be evaluated against the experimental data because it provided good enough results.

When comparing the CFD total pressure results from Grid 2 to the experimental data for the baseline nozzle, it was found that before x/Dh of 5, the computational values match the experimental throughout the centerline and the horizontal and vertical profiles. However, past x/Dh of 5 the computational values separate away from the experimental data but still display similar characteristics. This error could have been minimized if the values for Grid 3 would have been evaluated past x/Dh of 5 or by increasing the length of the viscous block to be closer to x/Dh of 10.

For the aft-deck configuration, the total pressure comparison showed that the data was consistent with the experimental values. The horizontal values at each x/Dh location were more consistent with the experimental data than the vertical values. The reason for this was because the T-Rex method that was used to build the viscous block from the deck caused some inconsistent cell spacing in the vertical direction. The static pressure distribution showed that the surface domain

on the deck was fine enough to provide good values across each point. In order to increase the accuracy of the aft-deck, the grid could have been generated using a symmetry line which would provide the same number of points but double the definition.

In conclusion, the data from the CFD analysis will be used by the Air Breathing Propulsion System Integration Technical Committee to check the accuracy of different CFD solvers and methods. They will use that information to improve current CFD techniques for future use in the industry. Recommendations and further research include improving the length of the viscous layer from x/Dh of 5 to x/Dh of 10 to increase the definition further into the farfield. Also, using a structured grid on the nozzle configuration to see the difference in the data that it received. Different solving methods ca be used to check the difference in values from one solver to another to see which techniques work best for this system.

References

1. https://paw.larc.nasa.gov/. 4th PAW Nozzle Guidelines

2. Parviz Behrouzi and James J. McGuirk. "Underexpanded Jet Development from a Rectangular Nozzle with Aft-Deck", AIAA Journal, Vol. 53, No. 5 (2015), pp. 1287-1298.

3. Anderson, John David. *Computational Fluid Dynamics: The Basics with Applications*. McGraw-Hill, 1995.

4. *NASA*, NASA, www.grc.nasa.gov/www/k-12/airplane/tunnel1.html.

5. Versteeg, H. K., and W. Malalasekera. *An Introduction to Computational Fluid Dynamics: the Finite Volume Method*. Pearson Education Ltd., 2007.

6. Farrashkhalvat, M., and J. P. Miles. *Structured Grid Generation: with an Introduction to Unstructured Grid Generation*. Butterworth-Heinemann, 2003.

7. "Quality and Control - Two Reasons Why Structured Grids Aren't Going Away | The Connector." *Quality and Control - Two Reasons Why Structured Grids Aren't Going Away | The Connector*, www.pointwise.com/theconnector/2013-March/Quality-Control-Two-Reasons-Structured-Grids-Arent-Going-Away.html.

8. Sreenivas, Kidambi & Mittal, Anshul & Hereth, Levi & Taylor, Lafayette. (2015). Computational Simulation of the Interaction between Tandem Wind Turbines with Offset. 10.2514/6.2015-0224.